Materials Horizons

ROYAL SOCIETY OF CHEMISTRY

COMMUNICATION

View Article Online
View Journal

Cite this: DOI: 10.1039/d6mh00152a

Received 27th January 2026,
Accepted 22nd April 2026

DOI: 10.1039/d6mh00152a

rsc.li/materials-horizons

Atomically dispersed Ru on defective CdS for photocatalytic solar fuel production coupled with hydrazine degradation

Zikang Zeng,[a] Siyu Kang,[a] Xiaohe Jiang,[a] Hai Qiu,[b] Yu-Chia Chang,[c] Yu-Ting Chueh,[c] Lan Yuan, *[b] Yujun Liang, [a] Jianguo Chang,*[d] Gui Yang,[e] Sung-Fu Hung *[c] and Chuang Han *[a]

Photocatalytic solar fuel production offers a sustainable approach for generating renewable feedstocks. However, this promising strategy is often hindered by the sluggish reaction kinetics and undesired CO_2 emission. In this study, we develop a CdS-Ru photocatalyst through the introduction of sulfur vacancy and atomically dispersed Ru sites into defective CdS. This design promotes directional charge transfer and forms highly active redox centers. Further leveraging the distinctive kinetic and thermodynamic features of hydrazine oxidation as a chemical regulation strategy, we establish a dual-functional paradigm that couples solar fuel production with hydrazine degradation. The CdS-Ru photocatalyst achieves hydrogen evolution and methanol production rates of 212.7 mmol g^{-1} h^{-1} and 1.4 mmol g^{-1} h^{-1}, respectively. It shows a substantial improvement over pristine CdS, and outperforms the systems employing conventional sacrificial reagents, such as triethanolamine or sulfides. Notably, this process yields no carbon-based byproducts (*e.g.*, CO, CO_2, and formaldehyde), ensuring a cleaner fuel production pathway. Comprehensive experimental analyses and theoretical simulations are conducted to elucidate the structural and electronic properties of the CdS-Ru catalyst, as well as the working mechanism of redox coupling, providing new insights for constructing dual-functional photocatalysts to tackle environmental and energy crises.

New concepts

This work demonstrates a novel dual-functional photocatalytic paradigm that couples efficient solar fuel production (H_2 and CH_3OH) with the complete degradation of the hazardous pollutant hydrazine (N_2H_4), achieving a zero-carbon-emission process. This concept fundamentally diverges from conventional systems that rely on organic sacrificial agents (*e.g.*, TEOA, alcohols), which inevitably generate carbonaceous byproducts (CO_2, formaldehyde) and complicate reaction mechanisms. The breakthrough is enabled by a rationally designed CdS-Ru catalyst, where sulfur vacancy and atomically dispersed Ru sites synergistically regulate directional charge transfer and optimize molecular adsorption, ensuring stoichiometric N_2H_4 oxidation to N_2 without ammonia byproducts. This strategy establishes a new design principle for multifunctional photocatalytic system to address intertwined energy and environmental challenges, moving beyond the traditional paradigm of merely scavenging holes with organic sacrificial reagents.

1. Introduction

Solar-driven H_2O splitting, CO_2 or N_2 reduction for the production of energy-rich chemicals, *i.e.*, solar fuel production, has been widely regarded as a promising route to meet the growing global energy demand while mitigating environmental concerns.[1] However, the efficiency of solar-to-chemical energy conversion is significantly constrained by sluggish surface reaction kinetics on semiconductor materials.[2,3] In particular, the extraction and utilization of photoexcited holes typically occur at a much faster rate than the corresponding electron-driven photophysical and photochemical processes.[4] To reconcile the competing requirements of light absorption, charge carrier separation, and surface reaction kinetics, traditional photocatalytic systems often employ sacrificial agents such as triethanolamine (TEOA), ascorbic acid, sulfides, alcohols, and amines to scavenge photogenerated holes, as dipicted in Scheme 1a.[5,6] Despite their widespread use, these scavengers still demand energetically favorable holes for oxidation and often lead to the generation of reactive intermediates and carbonaceous byproducts,[7] including CO_2 and formaldehyde.[8] Such byproducts not only complicate the reaction mechanisms

[a] Faculty of Materials Science and Chemistry, China University of Geosciences, Wuhan, 430074, China. E-mail: hanc@cug.edu.cn
[b] Key Laboratory of Hubei Province for Coal Conversion and New Carbon Materials, Wuhan University of Science and Technology, Wuhan, 430081, China. E-mail: yuanlan@wust.edu.cn
[c] Department of Applied Chemistry, National Yang Ming Chiao Tung University, Hsinchu, 300, Taiwan. E-mail: sungfuhung@nycu.edu.tw
[d] Faculty of Anhui Key Laboratory of Green Carbon Chemistry, Fuyang Normal University, Fuyang, 236037, China. E-mail: jgchang@fynu.edu.cn
[e] Faculty of Environmental Science and Engineering, Kunming University of Science and Technology, Kunming, 650500, China

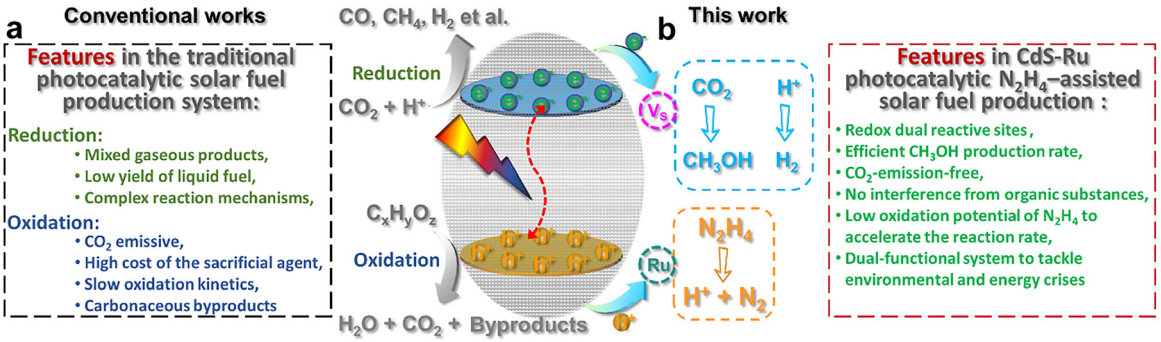

Scheme 1 (a) Features of traditional photocatalytic solar fuel production system. (b) Features of CdS-Ru photocatalytic N_2H_4-assisted solar fuel production system.

but also compromise the long-term stability of the semiconductor photocatalysts, thereby posing significant challenges to the development of durable and efficient photocatalytic systems.[9,10]

Ammonia (NH_3), a readily oxidizable inorganic molecule with a high hydrogen storage density, has recently emerged as a promising hole scavenger for photocatalytic hydrogen production. Its low oxidation potential (+0.02 V *vs.* RHE) and the benign nature of its oxidation byproducts make it particularly attractive for sustainable applications.[11] However, hydrazine (N_2H_4) offers even greater potential due to its significantly lower oxidation potential (−0.33 V *vs.* RHE) and reduced tendency to poison catalysts.[12] These advantages have spurred increasing interest in employing the hydrazine oxidation reaction (HzOR) to replace the inherently sluggish water oxidation (+1.23 V *vs.* RHE) in electrocatalytic hydrogen production systems.[13,14] Moreover, hydrazine is a recognized environmental pollutant commonly detected in wastewater from the chemical, pharmaceutical, aerospace, and nuclear industries. Its high solubility (reaching 1400–1700 mg L^{-1} in certain industrial effluents),[15,16] inherent alkalinity, and substantial chemical oxygen demand (COD) significantly complicate its removal from contaminated streams.[17–20] Although hydrazine commands a higher market price compared to conventional sacrificial agents or solar fuels (*e.g.*, H_2, methanol and NH_3),[13,14] its status as a highly toxic and carcinogenic substance necessitates the urgent development of effective degradation strategies.[17,21,22] In this context, we propose that photocatalytic hydrazine decomposition represents a dual-purpose strategy, simultaneously enabling the environmentally responsible degradation of hazardous hydrazine and facilitating the generation of solar fuels (Scheme 1b). This approach not only enhances photocatalytic efficiency but also aligns with broader goals of environmental remediation and sustainable energy production.

The oxidation of hydrazine by photogenerated holes yields N_2 as the sole product, avoiding the emission of carbon-containing species such as CO, CO_2, or formaldehyde. This eliminates complications in interpreting catalytic mechanisms that often arise from the decomposition of organic sacrificial agents.[17,23,24] Particularly, carbonaceous oxidation can produce C1 or related products during photocatalytic CO_2 reduction, potentially resulting in ambiguous or overstated performance claims.[25] Additionally, the inherent alkalinity and low oxidation potential of hydrazine could enhance the solubility of CO_2 in aqueous media and help prevent over-oxidation of the reduction products.[26] Importantly, the resulting mixture of N_2 and solar fuels poses no significant safety risks. Indeed, the carbon-free feature of hydrazine already make it attractive in zero-carbon emission H_2 fuel production through electrocatalysis,[27] while hydrazine remains underexplored in photocatalytic systems.

Ruthenium (Ru) has demonstrated high activity for the hydrazine oxidation reaction (HzOR), primarily due to the strong orbital interaction between N 2p and Ru 3d orbitals.[28] However, conventional Ru nanoparticles often fail to achieve complete oxidation of hydrazine, leading to the formation of undesired byproducts such as ammonia.[18] Furthermore, given the limited availability and high cost of Ru, it is desired to develop photocatalysts with high mass activity to minimize the required loading of this noble metal.[29,30] In this sense, engineered Ru single-atom catalysts offer a promising strategy, as their excellent dispersion and full accessibility of active sites can significantly enhance photocatalytic efficiency.[31] Pioneering works suggested that transition metal sulfide semiconductors are promising platforms for engineering photocatalysts with atomically dispersed reactive sites,[32–34] due to the structure self-adapting reconstruction and defect-oriented coordination features. For instance, Liu *et al.* synergistically introduced S vacancy (V_S) with atomic Cu into $ZnIn_2S_4$ nanosheets to tune the charge separation and modulate gradient hydrogen migration for enhancing photocatalytic H_2 production.[32] Zhou *et al.* reported a strategy for modulating surface electron density and reactant adsorption manner by regulating a single Au atom in defective CdS for effective CO_2 photoreduction.[35] We envision that the dynamic charge transfer between isolated Ru atoms and the defective semiconductor substrate, along with the tunable coordination environment of Ru centers, can be leveraged to optimize the delocalized electron distribution and the adsorption behavior of hydrazine and related species. This, in turn, may facilitate the complete oxidation of hydrazine and improve overall solar fuel production performance.

Herein, we developed a photocatalytic system by incorporating atomically dispersed Ru into a defective CdS semiconductor (CdS-Ru) to enable zero-carbon-emission solar fuel production *via* coupled hydrazine degradation. CdS was selected to be a

model semiconductor due to its simple structure, readily accessible vacancies, and favorable visible light harvesting. A combination of experimental investigations and density functional theory (DFT) calculations revealed that interfacial charge transfer and optimized molecular adsorption, regulated by V_S and atomically dispersed Ru active sites, play key roles in facilitating the complete dehydrogenation of hydrazine. This process results in the stoichiometric generation of reductive products (H_2 or CH_3OH) and the oxidative product (N_2). The rationally designed CdS-Ru catalyst and the comprehensive investigation of its catalytic behavior in hydrazine-assisted solar fuel production offer valuable insights into the photocatalytic elimination of nitrogen-based pollutants and the development of clean energy production technologies.

2. Experimental section

2.1. Synthesis of CdS and CdS-Ru

Uniform CdS nanowires (NWs) were prepared through a solvothermal method.[36] The detailed processes were described in supporting information. Atomically dispersed Ru-modified CdS (CdS-Ru) was synthesized *via* a facile wet-chemical process, as depicted in Fig. 1a. Specially, cadmium diethyldithiocarbamate ($Cd(S_2CNEt_2)_2$) was firstly prepared by precipitating the mixture of sodium diethyldithiocarbamate trihydrate (DDTC) and cadmium chloride ($CdCl_2$) in deionized water. Then 0.843 g $Cd(S_2CNEt_2)_2$and a certain amount of $RuCl_3{\cdot}3H_2O$ was added to a 50 mL capacity Teflon-lined stainless steel autoclave, followed by filling the autoclave with 30 mL of diethylamin. The autoclave was maintained at 180 °C for 24 h and subsequently cooled to room temperature. The resulting yellow precipitate was collected and washed with anhydrous ethanol and deionized water to remove residual organic solvents. The final product was dried in an oven at 60 °C for 12 h. The actual content of Ru (wt%) in different samples was checked through inductively coupled plasma-mass spectrometry (ICP-MS, Agilent 7900) and the results are shown in Table S1. Since the photocatalytic activity of CdS-$Ru_{0.18}$ is highest among these samples, without special mention, the CdS-Ru refers to CdS-$Ru_{0.18}$ sample in the subsequent discussion.

2.2 Photoactivity test

The photocatalytic H_2 production tests were conducted in a 50 mL quartz reactor equipped with circulating condensate water (10 °C), with a solvent of 10 mL aqueous solution of different concentrations (wt%) of hydrazine hydrate, and a certain amount of catalyst was added to the solution system. After ultrasound dispersion, the reaction tube was purged with argon gas for 15 minutes to remove air, and then transferred to

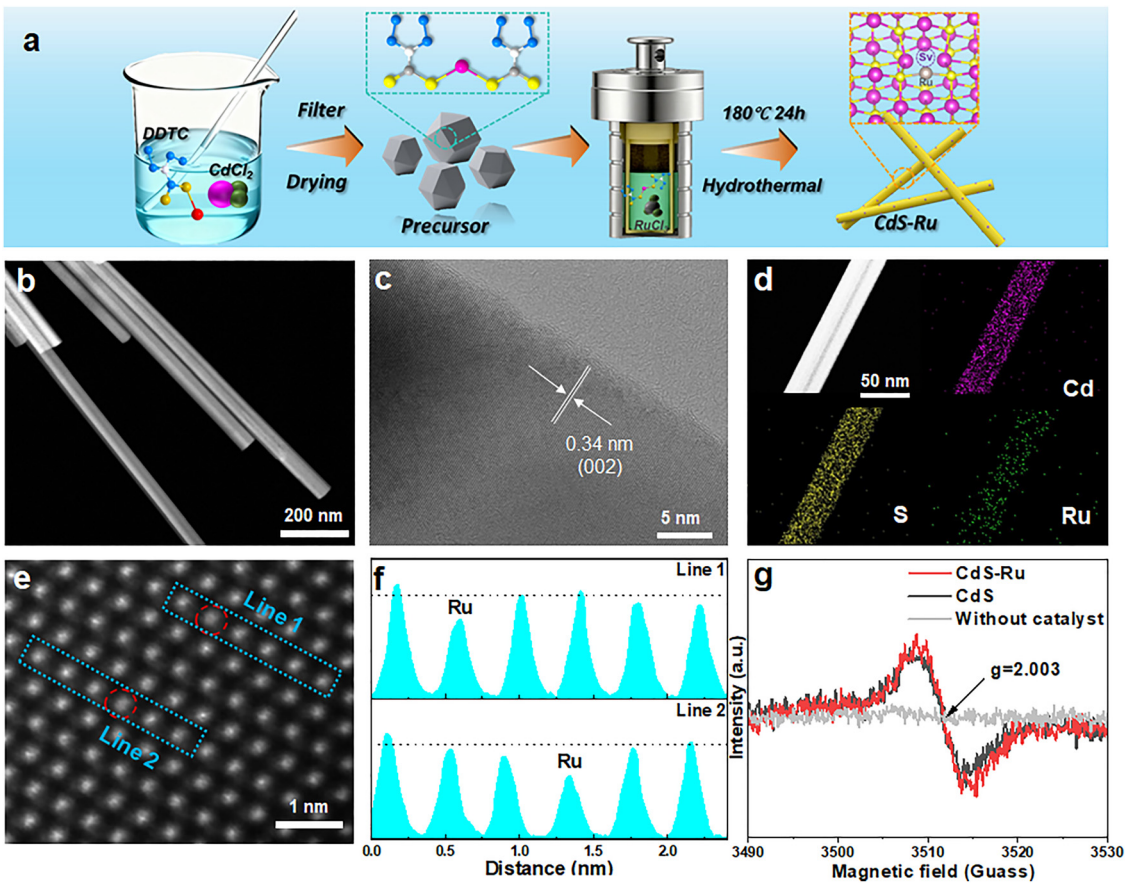

Fig. 1 (a) Schematic illustration of the synthesis of CdS-Ru. (b) TEM, (c) HRTEM, (d) elemental mapping and (e) aberration-corrected HAADF-STEM images of CdS-Ru. f) Corresponding line-scan profiles marked in (e) with line 1 and line 2. (g) EPR curves of CdS, CdS-Ru and background.

illumination under light emitting diode (LED, $\lambda > 400$ nm, 60 mW cm^{-2}) lamp or 300 W Xe ($\lambda > 420$ nm, 200 mW cm^{-2}) lamp to investigate the photocatalytic H_2 production performance of the catalyst under weak and strong light conditions. The rotational speed was fixed at 500 rpm during testing. The produced gas was analyzed using gas chromatography. For stability testing, the recovered catalyst was filtered using nylon filter paper and then dried at 60 °C.

For CO_2 photoreduction, 2 mg of catalyst and 10 mL of distilled H_2O containing 2 wt% hydrazine hydrate were mixed in a quartz reactor (25 mL) equipped with circulating condensate water (10 °C) to form suspensions. The suspension was then purged with CO_2 (or Ar) gas for 10 min. A Xe lamp ($\lambda > 420$ nm) was used as the irradiation source. The energy output is 200 mW cm^{-2} measured by an optical power/energy meter (Newport 842-PE). During photocatalysis, the suspension was continuously stirred to ensure uniform irradiation. The evolved gases were analyzed using a gas chromatograph (Shimadzu GC-2014C, MS-5 A column, Ar carrier) equipped with a thermal conductivity detector (TCD) and a flame ionization detector (FID). Products in solution were analyzed on a gas chromatograph (Shimadzu GC-2014C, GDX-502 column, Ar carrier) and quantified using a Shimadzu TQ8040 gas chromatography-mass spectrometry (GC-MS). The liquid products were also qualitative by nuclear magnetic resonance (NMR, Bruker Avance, 600 MHz). The selectivity of CH_3OH was calculated according to the following formula:[37]

$$CH_3OH\ \text{selectivity}\ (\%) = \frac{n(CH_3OH)}{n(CO) + n(CH_3OH)} \times 100\%$$

3. Results and discussion

3.1. Preparation and structure characterizations

Atomically dispersed Ru-modified CdS (CdS-Ru) was synthesized *via* a facile two-step process, as depicted in Fig. 1a. The CdS precursor exhibited an irregular lump-like morphology (Fig. S1), whereas both CdS and CdS-Ru showed uniform one-dimensional (1D) nanowire (NW) structures with an average diameter of approximately 40 nm, as confirmed in Fig. 1b and further detailed in Fig. S2. The length of NWs was extended to several micrometers. High-resolution transmission electron microscopy (HRTEM) characterization of CdS-Ru revealed well-defined lattice fringes with a spacing of 0.34 nm, corresponding to the (002) crystal plane of hexagonal CdS (Fig. 1c). Notably, no Ru/RuS_x nanoparticles or nanoclusters were observed on the surface of CdS NWs, even in the sample with the highest Ru doping content (Fig. S2–S4). Elemental mapping of Ru (Fig. 1d, Fig. S3 and S4) confirmed its uniform distribution, suggesting a high degree of atomic dispersion. Aberration-corrected high-angle annular dark field scanning TEM (HAADF-STEM) was employed (Fig. 1e), revealing that the ordered arranged metal atoms have different brightness.[38] The line-intensity profile marked with blue shows that Ru atoms appear on Cd atom row arrays (Fig. 1f), which indicates that Ru atom is replacing the Cd site of CdS.[39] The substitutional structure was further jointly corroborated by the following X-ray diffraction (XRD), electron paramagnetic resonance (EPR), and X-ray absorption spectroscopy (XAS) measurements.

The crystal structures of CdS and CdS-Ru were determined by X-ray diffraction (XRD). All samples exhibited diffraction patterns corresponding exclusively to the hexagonal CdS phase (PDF#41-1049), as shown in Fig. S5. A comparison of the XRD peak positions between CdS and CdS-Ru with different Ru loading contents reveals a slight negative shift upon Ru incorporation (Fig. S6), which can be attributed to lattice distortions induced by the embedded Ru species.[32] Electron paramagnetic resonance (EPR) measurements further confirmed structural modifications, with a pronounced signal at $g = 2.003$ in both CdS and CdS-Ru, characteristic of V_S (Fig. 1g).[32] Given the similar ionic radii of Ru and Cd, the incorporation of Ru into the CdS lattice is expected to cause only modest structural perturbations, consistent with the slightly enhanced EPR signal intensity observed for CdS-Ru. This suggests that atomically dispersed Ru and sulfur vacancies coexist in the catalyst, collectively contributing to the modification of the local electronic structure. X-ray photoelectron spectroscopy (XPS) was employed to characterize the elemental composition and electronic interactions. The survey spectra confirmed the presence of Cd and S in both CdS and CdS-Ru (Fig. 2a). High-resolution XPS of Cd 3d (Fig. 2b) and S 2p (Fig. 2c) confirm the expected oxidation states of Cd^{2+} and S^{2-} in the CdS lattice. The slightly higher intensity observed for CdS-Ru, combined with the positive shifts in Cd 3d and S 2p binding energies after Ru incorporation, suggests that Ru atoms substitute into the CdS lattice and modulate the local electronic environment, with sulfur vacancies present in the vicinity. Although the Ru signal in CdS-Ru is weak due to the low content and atomic dispersion of Ru (Fig. S7), the observed positive shifts in the binding energies of both Cd and S after Ru incorporation indicate a strong electronic interaction between Ru atoms and the CdS matrix.[40]

To further elucidate the structure and coordination environment of the Ru species in CdS-Ru, X-ray absorption spectroscopy (XAS) was performed. X-ray absorption near-edge structure (XANES) analysis (Fig. 2d) indicates that the average oxidation state of Ru in CdS-Ru lies between that of metallic Ru (Ru foil) and the Ru^{4+} in RuS_2, suggesting a partially oxidation state for the atomically dispersed Ru species.[31] The Fourier transform of the extended X-ray absorption fine structure (EXAFS) spectra (Fig. 2e) shows a prominent peak at 1.84 Å, which can be ascribed to the Ru–S coordination bond.[41] Notably, there is no observable peak corresponding to Ru–Ru bonding (2.39 Å), providing strong evidence for the atomic dispersion of Ru within CdS matrix. Quantitative EXAFS fitting (Fig. 2f and Table S2) estimates the Ru–S coordination number to be *ca.* 3, suggesting that each Ru atom is coordinated to three sulfur atoms. Wavelet transform (WT) EXAFS analysis further corroborates this finding. The dominant WT intensity for CdS-Ru appears at 8.0 $Å^{-1}$ (Fig. 2g–i), positioned between the reference signals of Ru foil and RuS_2. This spatial frequency is characteristic of Ru–S coordination and visually confirms the absence of Ru–Ru interactions, reinforcing the conclusion that Ru species are atomically dispersed on the CdS support.[42]

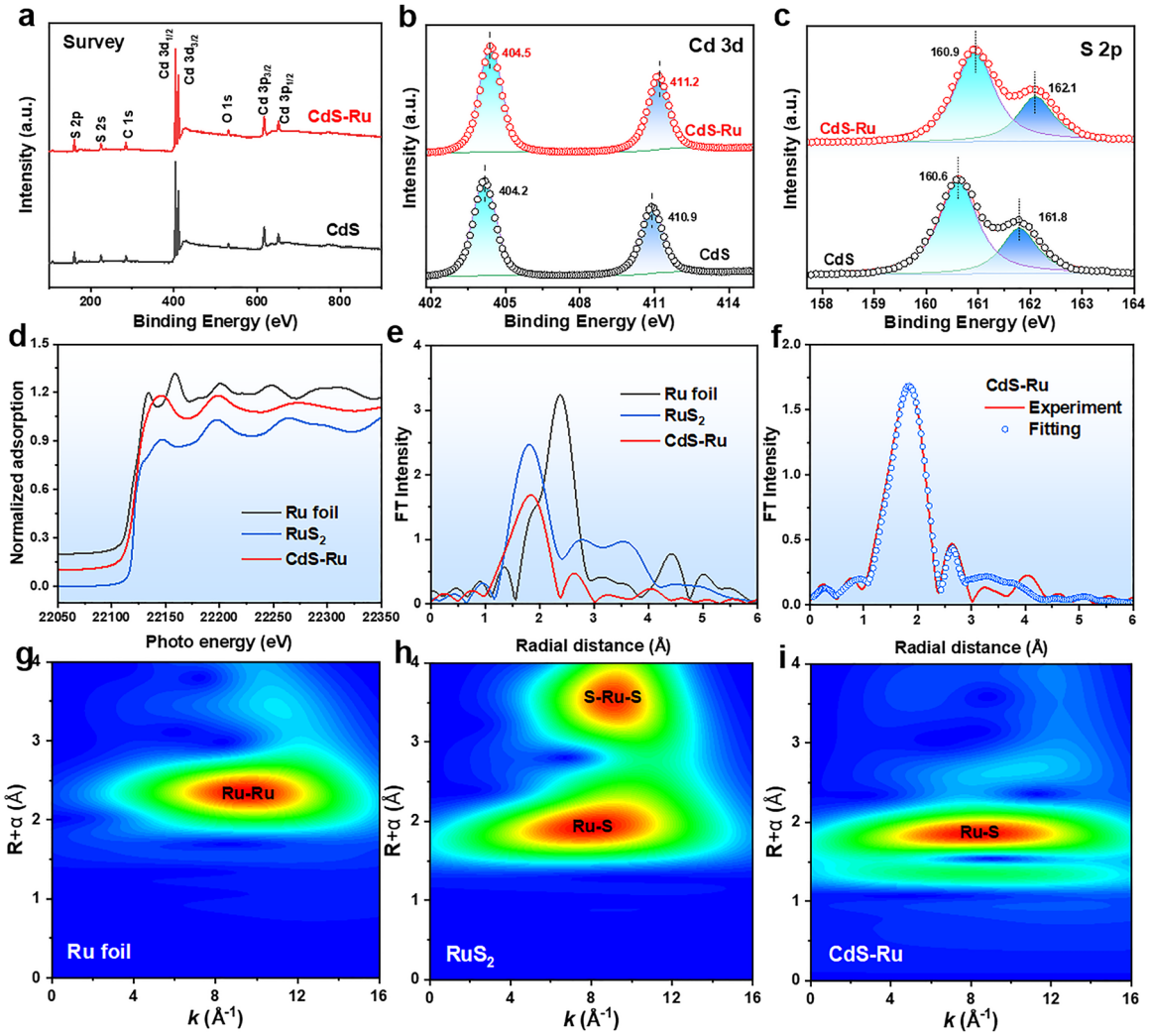

Fig. 2 (a) XPS survey spectrum for CdS and CdS-Ru. (b) High-resolution XPS spectra of Cd 3d and (c) S 2p spectra in CdS and CdS-Ru. (d) XANES and (e) EXAFS spectra of CdS-Ru (Ru foil and RuS_2 were applied for comparison). (f) Fit of the EXAFS signals of CdS-Ru at the Ru R edge. (g–i) Wavelet transform of the k^3-weighted EXAFS signal at Ru K-edge of Ru foil, RuS_2 and CdS-Ru.

3.2. Photocatalytic solar fuel production coupled with hydrazine degradation

The photocatalytic performance of CdS-Ru was evaluated separately in terms of both H_2 evolution and CO_2 reduction. The photocatalytic performance of H_2 evolution coupled with hydrazine degradation was initially evaluated for CdS and CdS-Ru samples with varying Ru loading. As shown in Fig. S8, the CdS-Ru loaded with 0.18 wt% Ru disclosed the highest H_2 production rate, benefiting from the efficient separation and transfer efficiency of charge carriers, as will be discussed later. After further optimizing reaction conditions (Fig. S9), including hydrazine concentration and catalyst feeding, the CdS-Ru sample achieved a maximum H_2 production rate of 46.1 mmol g^{-1} h^{-1} under 60 mW cm^{-2} white light emitting diode illumination (LED, $\lambda > 400$ nm). This rate is 46 times higher than that of pristine CdS, which produced only 1.0 mmol g^{-1} h^{-1}. To check whether the H_2 evolution process is driven by photocatalysis, controlled experiments were conducted. As shown in Fig. 3a and Fig. S10, the H_2 evolution over CdS-Ru increases steadily during continuous light irradiation. No H_2 generation was observed in the absence of either light or catalyst. In addition, using an equal molar amount of $RuCl_3$ as that in CdS-Ru for the reaction leads to no H_2 production (Fig. S11), confirming that the enhanced activity is both photocatalytic and catalyst-dependent. The apparent quantum efficiency (AQE) of CdS-Ru correlates well with its optical absorption spectrum (Fig. 3b), reinforcing that H_2 evolution is driven by photoexcitation. The highest AQE, recorded at 420 nm, reached 31.79%.

Recyclability tests demonstrated that CdS-Ru shows a stable H_2 evolution rate over multiple consecutive cycles (Fig. 3c), indicating excellent durability. Additionally, the sample stored *in situ* for 7 and 14 days retained its catalytic activity upon re-exposure to reaction conditions. Similar results were also observed in recycling tests performed under ambient conditions (Fig. S12). Post-reaction analyses, including structural (Fig. S13a), morphological (Fig. S13b and c), and composition (Fig. S14a and b) characterizations,

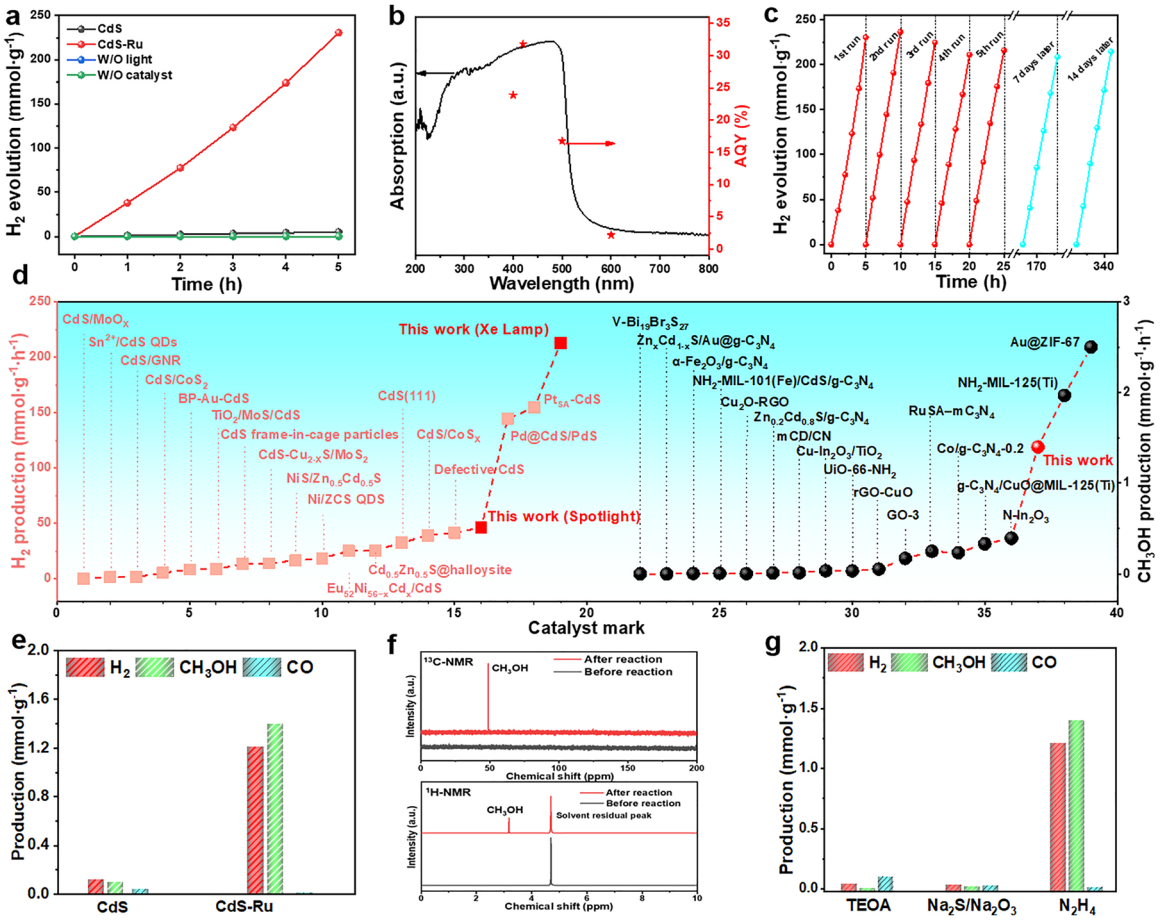

Fig. 3 (a) H_2 evolution performance of different photocatalysts under LED light irradiation (60 mW cm^{-2}, $\lambda > 400$ nm) or dark conditions. (b) AQE testing for H_2 evolution over CdS-Ru. (c) The stability testing of CdS-Ru for photocatalytic H_2 evolution. Reaction conditions in a-c: 2 mg catalyst, 10 mL 2 wt% hydrazine hydrate. (d) Comparison of H_2 and methanol production activity over different photocatalysts. The detailed information corresponding to different catalyst marks was disclosed in Tables S3 and S4. (e) The photocatalytic CO_2 reduction performance of CdS-Ru and CdS under Xe lamp (200 mW cm^{-2}, $\lambda > 420$ nm). Reaction conditions: 2 mg catalyst, 10 mL 2 wt% hydrazine hydrate. (f) ^{13}C-NMR and ^{1}H-NMR spectra before and after the photocatalytic CO_2 reduction with CdS-Ru. (g) Photocatalytic CO_2 reduction with CdS-Ru and different sacrificial agents.

confirmed that the CdS-Ru catalyst remained unchanged, further evidencing its structural stability and robustness. Although trace amounts of Cd–O or Cd–OH species might be formed on the catalyst surface after prolonged reaction, their concentration is below the detection limit of XPS and thus not observable in the Cd 3d spectrum. XANES and EXAFS analyses were performed on the Ru sites after the reaction. As shown in Fig. S15, the coordination environment of Ru remained largely unchanged after the reaction, while a slight positive shift in oxidation state was observed, which can be attributed to hole accumulation at the Ru sites due to the occurrence of reduction reactions. ICP-MS analysis of the recovered CdS-Ru after seven cycles (35 h) showed that the Ru content remained 0.18 wt% (Table S3), identical to the fresh catalyst, and the reaction solution contained only 0.008 mg L^{-1} Cd, corresponding to dissolution of merely 0.005% of the total CdS. This trace Cd leaching is attributed to the gradual consumption of hydrazine, which serves as the hole scavenger. After 35 h of cycling, approximately 25.8% of the initial hydrazine (51.7 mg out of 200 mg) is consumed. As the concentration of hydrazine decreases, a fraction of photogenerated holes cannot be promptly quenched, leading to mild photooxidation of the CdS lattice and resulting in trace Cd^{2+} release. Furthermore, ICP-MS analysis of the reaction solution after a single 5 h photocatalytic cycle revealed a cadmium leaching concentration below 0.001 mg L^{-1}, which is within the WHO guideline limit for drinking water (< 0.003 mg L^{-1}).[43] After seven consecutive cycles over 14 days (total 35 h of reaction), the cumulative cadmium concentration reached 0.008 mg L^{-1}. No detectable ruthenium leaching was observed. While these results confirm good stability under typical operating conditions, prolonged use of CdS-based photocatalysts may lead to cumulative cadmium release, underscoring the need for developing cadmium-free alternatives. The inhibition of photocorrosion and good stability of CdS-Ru may be benefited from the relatively lower oxidation potential and carbon-free features of hydrazine, which hinder the generation of oxidative and poisonous species.

To further highlight the advantages of CdS-Ru, *in situ* photodeposition of Ru and Pt onto CdS was performed, a widely recognized benchmark method for preparing efficient photocatalysts for H_2 evolution.[44] As shown in Fig. S16, CdS-Ru significantly outperforms both Ru- and Pt-photodeposited CdS

samples in terms of H_2 generation rate, demonstrating the superior catalytic efficiency of atomically dispersed Ru sites. Moreover, control experiments were conducted to evaluate H_2 evolution activity in the presence of alternative sacrificial agents, including CH_3OH, TEOA, and Na_2S/Na_2SO_3 (Fig. S17). Among these, the hydrazine-assisted system showed the highest photoactivity, indicating its effectiveness as a hole scavenger. Collectively, these results confirm the synergistic effect between atomically dispersed Ru sites and hydrazine in enhancing H_2 evolution performance, supporting the rational design of the CdS-Ru system for efficient photocatalytic solar fuel production.[19]

For a more comprehensive comparison with other catalysts, the photocatalytic performance of CdS-Ru was further evaluated under a Xe lamp (200 mW cm^{-2}, $\lambda > 420$ nm) or natural sunlight (Fig. S18). The H_2 evolution rates were measured to be 212.7 mmol g^{-1} h^{-1} and 60.2 mmol g^{-1} h^{-1} under Xe lamp and natural sunlight, respectively. Notably, the H_2 production rates achieved by CdS-Ru suppress that of many state-of-the-art H_2 evolution systems based on transition metal sulfide photocatalysts, as illustrated in Fig. 3d and detailed in Table S3. Upon Xe lamp illumination, rapid bubble formation was observed within seconds (Fig. S19), indicating the high efficiency of photocatalytic H_2 production coupled with hydrazine oxidation. Gas chromatography analysis of reaction products (Fig. S20) confirmed the exclusive formation of H_2 and N_2, with no detectable byproducts.[42] The measured molar ratio of N_2 to H_2 was *ca.* 1 : 2, consistent with the complete oxidation of hydrazine. These results collectively highlight the excellent photocatalytic performance and practical applicability of the CdS-Ru system for sustainable hydrogen production.

Building on the prominent photocatalytic H_2 evolution performance of the current reaction system, hydrazine-assisted CO_2 photoreduction was subsequently evaluated. As shown in Fig. 3e, CdS alone produced CH_3OH (0.11 mmol g^{-1} h^{-1}), CO (0.04 mmol g^{-1} h^{-1}), and H_2 (0.12 mmol g^{-1} h^{-1}), resulting in a relatively low CH_3OH selectivity of 77.3%. In contrast, CdS-Ru exhibited significantly enhanced performance, producing CH_3OH at 1.4 mmol g^{-1} h^{-1} and H_2 at 1.2 mmol g^{-1} h^{-1}, with a CH_3OH selectivity of 99.0% and AQE of 0.12% at 420 nm. Although current CO_2 reduction reaction system still suffers from the competitive H_2 evolution reaction, the markedly improved CH_3OH production rate and selectivity are superior to most reported data (Fig. 3d and Table S4).

Nuclear magnetic resonance (NMR) spectroscopy (Fig. 3f) confirmed that no other carbonaceous (C–N coupling) or NH_3 products were present in the liquid phase, supporting the conclusion that CH_3OH and H_2 are the dominant products. Notably, replacing hydrazine with a conventional scavenger such as TEOA or Na_2S/Na_2SO_3 led to a dramatic decline in photocatalytic activity, with CH_3OH becoming nearly undetectable (Fig. 3g). This pronounced difference is likely due to the low oxidation potential of hydrazine, which not only facilitates efficient separation of photoexcited charge carriers but also helps prevent overoxidation of CH_3OH, thereby enhancing product yield and selectivity.[45] The stability of CH_3OH production was also evaluated, with five consecutive cycles (25 h total) showing negligible activity loss (Fig. S21), confirming the excellent durability of CdS-Ru for CO_2 photoreduction.

To verify the origin of the products generated during solar fuel production, isotopic labeling experiments were conducted using $^{13}CO_2$ and/or D_2O as reactants. The resulting products were analyzed *via* gas chromatography-mass spectrometry (GC-MS). As shown in Fig. S22, when the $^{13}CO_2$ was used as the carbon source, the main mass fragment appeared at m/z = 33, corresponding to $^{13}CH_3OH$, confirming that the carbon in methanol originates from CO_2. When H_2O was further replaced with D_2O, the primary signal shifted to m/z = 37, consistent with the molecular weight of $^{13}CD_3OD$, indicating that the hydrogen in methanol is derived from water. In addition, the H_2 signal shifted to m/z = 4, confirming the formation of isotopically labeled D_2 gas. These results unambiguously demonstrate that the C in CH_3OH originates from CO_2, while the H in both H_2 and CH_3OH is sourced from H_2O, confirming the true solar-to-fuel conversion pathway.

3.3. Mechanism of photocatalytic performance enhancement

We next investigated the origin of the enhanced photocatalytic performance and the underlying reaction mechanism for solar fuel production coupled with hydrazine degradation. First, the optical absorption capacities of CdS and CdS-Ru were analyzed using ultraviolet–visible diffuse reflectance spectroscopy (UV-vis DRS). As shown in Fig. 4a, both materials exhibit similar optical bandgaps, indicating that Ru incorporation does not significantly alter the band structure of CdS. However, CdS-Ru displays a notably higher photoabsorption intensity compared to pristine CdS. While increasing the Ru content further enhances the absorption intensity (Fig. S23), it does not result in a corresponding improvement in photocatalytic activity. This observation suggests that the superior performance of CdS-Ru cannot be attributed solely to increased light absorption due to Ru incorporation. Therefore, other factors, such as improved charge separation, interfacial charge transfer, and catalytic site efficiency, likely play a more critical role in the observed enhancement.

To gain further insight into the enhanced photocatalytic performance, we investigated the charge carrier dynamics. Photoluminescence (PL) spectroscopy revealed that CdS-Ru exhibits a significantly lower PL intensity compared to pristine CdS (Fig. 4b and Fig. S24), indicating reduced radiative recombination of photoexcited charge carriers upon Ru loading. However, a high fraction of Ru incorporation can also lead to charge carrier recombination and result in decreased photocatalytic performance.[31] Time-resolved PL (TR-PL) spectroscopy with excitation at 400 nm and probe at 530 nm was then employed to quantify the charge carrier lifetimes (Fig. 4c). Based on the fitted results (Table S5), the average lifetime of charge carriers in CdS-Ru was found to be 2.71 ns, substantially longer than that of CdS (1.51 ns). This prolongation suggests more efficient charge separation and slower recombination processes in CdS-Ru sample. Furthermore, electrochemical impedance spectroscopy (EIS) was performed at reducing potentials of 0.3 V, −0.8 V and −0.9 V, with the results shown in Fig. 4d and Fig. S25. CdS-Ru exhibits a consistently smaller semicircle diameter than CdS at

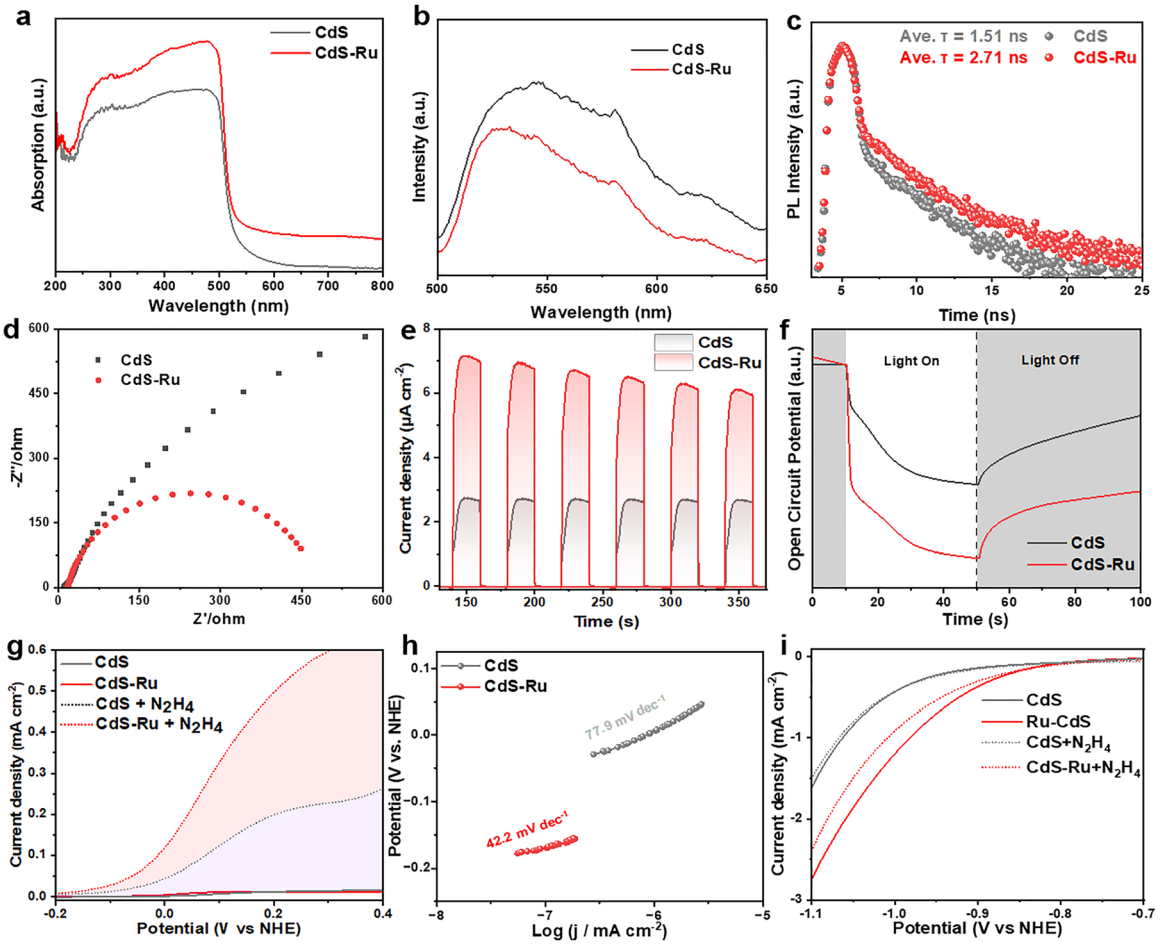

Fig. 4 (a) UV-vis DRS spectra, (b) PL spectra, (c) TR-PL spectra upon excitation at 400 nm, (d) EIS spectra tested at −0.8 V, (e) transient photocurrent response curves and (f) open-circuit voltage of CdS-Ru and CdS under a Xe lamp (200 mW cm^{-2}, $\lambda > 420$ nm) irradiation. (g) LSV curves and (h) Tafel slope of CdS and CdS-Ru for H_2O or N_2H_4 oxidation. (i) LSV curves of CdS and CdS-Ru for proton reduction.

both potentials, indicating lower charge transfer resistance and more efficient charge separation, which is in good agreement with the PL result in Fig. 4b. Moreover, as the applied potential becomes more extreme, the impedance of both electrodes decreases significantly, consistent with the trend reported.[46,47] Consistently, CdS-Ru displayed the highest photocurrent density among the samples (Fig. 4e), further confirming improved photo-induced charge separation and mobility. Generally, a larger potential difference (ΔE_{ph}) during light on/off indicates a higher accumulation of electrons. Therefore, the higher ΔE_{ph} of CdS-Ru can be attributed to the promotion of charge separation efficiency, which leads to a higher photovoltage (Fig. 4f). Collectively, these results demonstrate that the incorporation of atomically dispersed Ru sites facilitates more efficient charge transfer and separation, thereby contributing to the superior photocatalytic activity of the CdS-Ru system.[48]

To further elucidate the roles of Ru sites and hydrazine oxidation in influencing the kinetics of solar fuel production, linear sweep voltammetry (LSV) measurements were conducted. As shown in Fig. 4g, both CdS and CdS-Ru electrodes exhibit minimal current densities in 0.5 M Na_2SO_4 electrolyte without hydrazine, due to the high overpotential and sluggish kinetics associated with H_2O oxidation.[49,50] Upon the introduction of 1 mM hydrazine into the electrolyte, a sharp rise in responsive current is observed for both materials, with CdS-Ru showing a notably higher response than CdS. For example, at 0.1 V, CdS-Ru achieves a current density of 0.32 mA cm^{-2}, approximately 3 times greater than CdS (0.11 mA cm^{-2}) and 32 times higher than CdS-Ru in the absence of hydrazine (0.01 mA cm^{-2}). Tafel slope analysis was used to evaluate the kinetic behavior of the hydrazine oxidation reaction (HzOR). As presented in Fig. 4h, the Tafel slope for CdS-Ru is 42.2 mV dec^{-1}, significantly lower than that of CdS (77.9 mV dec^{-1}), indicating more favorable HzOR kinetics.[50] These results strongly suggest that the atomically dispersed Ru sites act as the primary active centers for promoting HzOR.[51]

The kinetics of the reduction half-reaction were also studied using LSV technology. As shown in Fig. 4i, the CdS-Ru electrode shows a reduced overpotential for H_2 evolution in comparison with pristine CdS, which correlates with the increased V_S density in CdS-Ru, as summarized in Table S6. This enhancement indicates that V_S and Ru sites contribute to improved catalytic activity for proton reduction. Despite the lower overpotential, the Tafel slope of CdS-Ru remains comparable to that of CdS (Fig. S26), manifesting that the rate-determining step is

still governed by surface adsorption/desorption processes, rather than charge transfer kinetics.[22] Interestingly, upon the addition of hydrazine into the Na_2SO_4 electrolyte, the current density of CdS-Ru decreases significantly, while that of CdS remains largely unaffected, which competitively inhibits the adsorption and reduction of protons.[52] This interaction and its mechanisms will be further elucidated through density functional theory (DFT) calculations in subsequent sections.

3.4. DFT calculations and *in situ* FTIR analysis

Density functional theory (DFT) calculations were performed to explore the electronic structure modifications induced by V_s and atomically dispersed Ru sites in the catalyst. All structural models were fully optimized, with the resulting geometries presented in Fig. S27. The optimized structure of CdS-Ru shows notable lattice distortions, attributed to the synergistic regulation of both atomic Ru and V_S sites. These computational results are consistent with experimental observations from XRD and ESR analyses. Density of states (DOS) analysis (Fig. 5a) reveals the emergence of mid-gap states near the Fermi level upon the incorporation of Ru and V_S, which are expected to enhance electrical conductivity and promote the separation of photogenerated electron–hole pairs.[53] Furthermore, the d-band center (ε_d) of CdS-Ru (3.28 eV) is shifted downward relative to that of CdS (3.47 eV), indicating an increased affinity for reactant adsorption, an effect corroborated by the adsorption energy (E_{ads}) calculations. As shown in Fig. 5b, hydrazine molecules interact with CdS and CdS-Ru through Cd–N and Ru–N bonding, yielding E_{ads} values of −1.42 eV and −1.47 eV, respectively. The more negative E_{ads} on CdS-Ru reflect stronger adsorption strength, which supports the experimentally observed complete oxidation of hydrazine on this catalyst. Similar trends were observed in the case of CO_2 adsorption. As depicted in Fig. 5c, CO_2 is only physically adsorbed on CdS, with a weakly positive E_{ads} of +0.47 eV. In contrast, on CdS-Ru, CO_2 undergoes significant molecular activation, as evidenced by bending and elongation of the O═C═O bond. The optimized structure shows that CO_2 is chemically adsorbed *via* two Cd atoms adjacent to the Ru and V_S sites, with an E_{ads} of −0.33 eV. These results further confirm the enhanced reactivity and activation capability of the CdS-Ru catalyst toward CO_2.

The direction of electron transfer and the site-specific charge accumulation behavior were further explored through surface electrostatic potential mapping (Fig. 5d). The analysis reveals that the V_S serves as an electron sink, directing the flow of electrons and inducing the redistribution of charge density. This results in localized electron accumulation on the surrounding Cd atoms (Fig. S28), which is beneficial for facilitating reduction reactions in solar fuel production. DOS calculations for hydrazine show a wide energy gap of *ca.* 7.5 eV, with the highest occupied molecular orbital (HOMO) located at about −5.1 eV (Fig. 5e). This HOMO level closely aligns with the valence band (VB) position of CdS (Fig. S29), suggesting the thermodynamic feasibility of hole transfer from CdS to hydrazine. Projected DOS analysis of CdS-Ru shows that Ru atoms contribute to the valence band maximum (VBM), implying that Ru sites are capable of accepting photo-induced holes from the CdS semiconductor.[54] Furthermore, there is a clear overlap between the DOS of hydrazine and the Ru 3d orbitals in CdS-Ru within the energy range corresponding to the HOMO of hydrazine (Fig. 5e). This suggests a favorable orbital interaction, enabling efficient hole transfer from photoexcited CdS-Ru to hydrazine *via* the Ru sites. Controlled experiment in the presence of $KBrO_3$ as the electron scavenger shows that only N_2 was produced from the hole oxidation of hydrazine (Fig. S30). Based on these findings, a comprehensive mechanism for charge carrier transfer and the associated redox reactions is proposed in

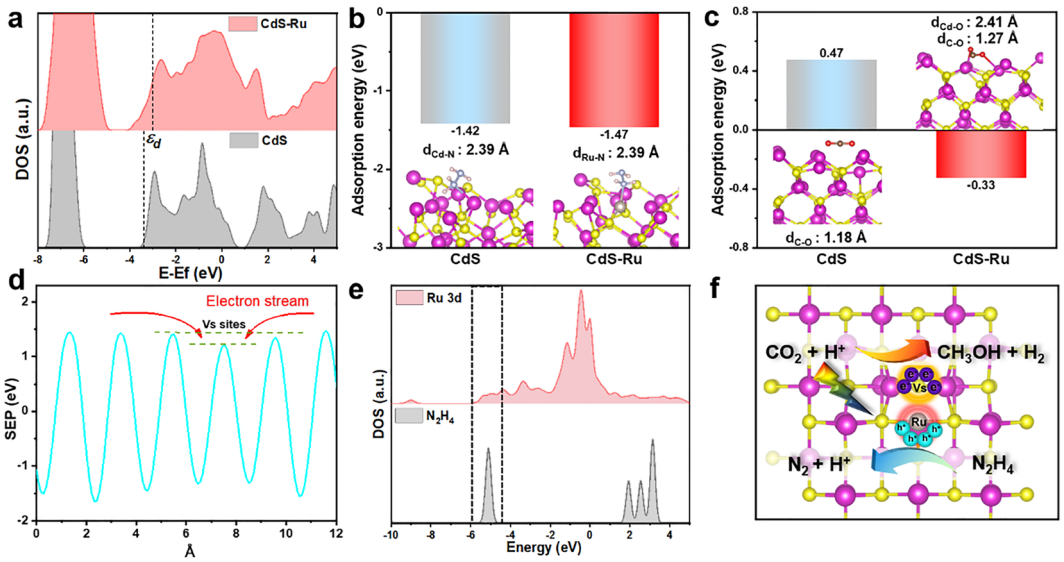

Fig. 5 (a) DOS and d-band center analysis on CdS-Ru and CdS. Adsorption energy of (b) N_2H_4 and (c) CO_2 on the CdS-Ru and CdS derived from DFT calculations. (d) Surface electrostatic potential on the S facet of CdS-Ru. (e) Comparison of projected DOS of Ru 3d in CdS-Ru and total DOS of N_2H_4. (f) Schematic illustration of charge transfer and solar fuel production coupled with hydrazine oxidation over CdS-Ru.

Fig. 5f. The diagram highlights the critical roles of V_S and atomically dispersed Ru sites in facilitating spatially separated charge transfer, promoting hydrazine oxidation and CO_2 (or H^+) reduction. This cooperative interaction highlights the chemical synergy essential for boosting solar fuel production.

To elucidate the detailed reaction mechanisms underlying solar fuel production and hydrazine degradation, free energy change (ΔG) calculations were performed. Fig. 6a shows the elementary reaction steps, corresponding energy profiles, and key intermediate configurations for CO_2 reduction and H_2 evolution. The CO_2 reduction pathway begins with the adsorption of CO_2 as *COOH (where * denotes an adsorbed species), a well-known, crucial intermediate in CO_2 conversion. The formation energy of COOH* on CdS-Ru is significantly lower (+0.02 eV) than that on CdS (+0.96 eV), which is attributed to the shift in the d-band center (ε_d) induced by Ru incorporation. This reduced energy barrier facilitates the initial CO_2 activation. Following *COOH formation, the elimination of OH to yield *CO (surface-bound carbonyl) is exothermic on both catalysts. The subsequent transformation of *CO plays a pivotal role in determining the product distribution. For CdS-Ru, the hydrogenation of *CO to *CHO is identified as the rate-determining step, with a ΔG of +0.61 eV lower than that of CdS (+0.77 eV). Moreover, the energy barrier for *CO desorption is higher than that for *CHO formation, suggesting that further hydrogenation toward CH_xO species and eventually CH_3OH is more favorable than CO adsorption.[55] This explains the enhanced CH_3OH selectivity observed experimentally (Fig. 3e). In the case of H_2 evolution, the green energy profile in Fig. 6a shows that CdS-Ru has a lower energy barrier (0.13 eV) compared to CdS (0.20 eV), consistent with LSV results (Fig. 4f). Notably, this moderate energy barrier closely matches that of CO_2 activation (0.15 eV), enabling concurrent formation of key intermediates for both H_2 production and CO_2 reduction, thereby contributing to the observed high activity and selectivity on CdS-Ru. While Ru is often recognized as an effective cocatalyst for water splitting due to its favorable water dissociation kinetics,[17] our calculations reveal a strong *H binding energy on Ru sites (0.74 eV, Fig. S31). This suggests that atomically dispersed Ru acts primarily active sites for HzOR. In summary, the free energy analysis confirms that the enhanced catalytic performance and CH_3OH selectivity of CdS-Ru arise from the favorable energetics of intermediate formation, efficient charge utilization, and the complementary roles of Ru and V_s in modulating reaction pathways.

The high selectivity toward CH_3OH and the absence of formic acid or formate can be attributed to the favorable energetics of the *CO hydrogenation pathway on CdS-Ru. The *COOH intermediate formed after CO_2 activation preferentially undergoes dehydration to form *CO rather than protonation to HCOOH, and the strongly adsorbed *CO is kinetically driven toward further hydrogenation to CH_3OH rather than desorption as CO or formate. This mechanistic preference, governed by the unique electronic structure of the catalyst, steers the CO_2 reduction pathway exclusively toward CH_3OH.

Given the limited research on hydrazine degradation over the photocatalysts,[19,56,57] it is essential to develop a deeper

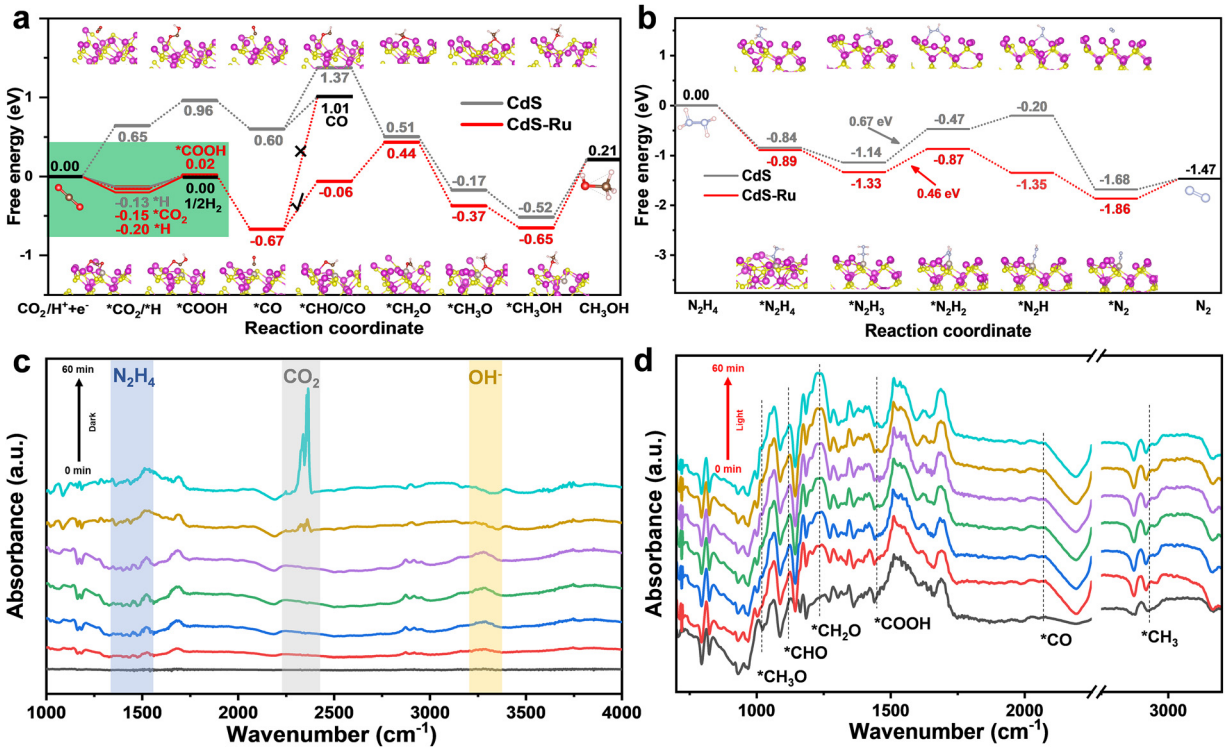

Fig. 6 (a) Free energy profiles for the H_2 evolution and CO_2 reduction over CdS-Ru and CdS. (b) Free energy profiles of N_2H_4 dehydrogenation oxidation over CdS-Ru and CdS. The insets of (a) and (b) show the corresponding structure models. *In situ* FT-IR spectra for co-adsorption of N_2H_4 and CO_2 on CdS-Ru (c) in the dark and (d) under visible light irradiation.

mechanistic understanding of dehydrogenation/oxidation kinetics of hydrazine. The reaction pathways for hydrazine degradation on CdS and CdS-Ru are demonstrated in Fig. 6b. Overall, the hydrazine degradation process is thermodynamically favorable and proceeds spontaneously in both systems. However, a key difference lies in the rate-determining step: the dehydrogenation of $*N_2H_3$ to $*N_2H_2$. This step presents an energy barrier of 0.46 eV on CdS-Ru, which is significantly lower than the 0.67 eV barrier observed on pristine CdS. Beyond this step, all subsequent elementary reactions on CdS-Ru are also exergonic, facilitating the complete multi-step dehydrogenation of hydrazine to N_2. In contrast, the CdS catalyst encounters an additional energy barrier of 0.27 eV during the conversion of $*N_2H_2$ to the next intermediate, further hindering the overall reaction kinetics. These findings highlight the critical role of atomically dispersed Ru sites in lowering kinetic barriers and promoting efficient, stepwise hydrazine dehydrogenation/oxidation. Together, these mechanistic insight highlights the catalytic advantage of CdS-Ru in enabling the complete and selective conversion of hydrazine to nitrogen, reinforcing its potential for use in photocatalytic pollutant degradation and solar fuel production.

To further elucidate the distinct roles of Ru and sulfur vacancies, we combined electronic structure analysis with reaction energy profiles. Surface electrostatic potential mapping (Fig. 5d) and charge distribution (Fig. S28) reveal that V_S induces electron accumulation on adjacent Cd atoms, creating reductive centers, while Ru sites exhibit strong orbital hybridization with the HOMO of N_2H_4 (Fig. 5e) and significantly lower the dehydrogenation barrier (Fig. 6b), confirming their function as oxidative centers. Moreover, *H adsorption on Ru is unfavorable (0.74 eV, Fig. S31), and *COOH formation, the key step in CO_2 reduction, occurs on Cd rather than Ru (Fig. 6a). These findings demonstrate a spatial separation of redox functions that Ru sites accelerate hydrazine oxidation, whereas electron-rich Cd sites adjacent to V_S promote CO_2 reduction and H_2 evolution. This synergistic cooperation underpins the high efficiency of the CdS-Ru system.

Finally, *in situ* FTIR spectra tests were conducted to confirm the proposed reaction pathway and intermediates. CO_2 and N_2H_4 were purged into the system in the dark, and the spectra were collected every 10 min. The accumulated intermediate species adsorbed on the surface of CdS-Ru can be identified from Fig. 6c. The bands in the range of 1300–1500 cm^{-1} indicate that the adsorption of N_2H_4 is associated with the wagging vibrational mode of the $-NH_2$ group in N_2H_4.[58] The peaks at approximately 2340 and 2360 cm^{-1} correspond to the adsorbed CO_2 on the surface of the catalyst.[59] The characteristic peaks of the adsorbed N_2H_4 and CO_2 are gradually enhanced, which leads to the intensity of surface OH^- species first increase, followed by a gradual decrease. This suggests that the presence of N_2H_4 may create more surface alkaline sites to promote the chemical adsorption of CO_2. Then the spectral signals under visible light irradiation were recorded with time interval of 10 min. As illustrated in Fig. 6d, new peaks attributed to reaction intermediates are emerged after light irradiation. The absorption bands of *COOH intermediate appear in the range of 1440–1460 cm^{-1}.[59] The linearly adsorbed *CO intermediate can be identified *via* the band at 2060 cm^{-1}.[60] The band at 1140 cm^{-1} corresponds to the characteristic peak of *CHO.[60] The characteristic band appearing at 1240 cm^{-1} is assigned to $*CH_2O$, while the band at 1020 cm^{-1} and 2960 cm^{-1} belong to the characteristic peak of $*CH_3O$ and $*CH_3$, which are the crucial intermediate for CO_2 reduction to methanol.[59–61] With the extension of irradiation time, the intensity of each characteristic peak gradually increased indicating the gradually hydrogenation of CO_2 to generate methanol. The key redox steps for the catalytic system were summarized in eqn (S1)–(S6).

4. Conclusions

In summary, we report the first successful integration of atomically dispersed Ru sites into CdS with V_S and systematically elucidate their structural and catalytic roles in solar fuel production coupled with hydrazine degradation. The synergistic presence of atomic Ru and V_S enables regional and directional separation of photoexcited charge carriers, driving oxidative reactions at Ru sites and reductive reactions at adjacent regions, thereby enhancing overall catalytic efficiency. Employing hydrazine as a hole scavenger not only circumvents the sluggish kinetics associated with water oxidation but also eliminates carbon emissions, making the process environmentally benign. Owing to this dual-site and chemical synergy, the CdS-Ru system demonstrates significantly improved photocatalytic activity for both H_2 evolution and CO_2 reduction to CH_3OH, while achieving complete oxidation of toxic hydrazine to N_2. This work offers valuable insights into the rational design of multifunctional photocatalysts and integrated reaction strategies for achieving efficient solar fuel production with added environmental benefits, paving the way for sustainable and clean energy technologies.

Author contributions

Zikang Zeng: writing – original draft, methodology, investigation, data curation, conceptualization. Siyu Kang: methodology, data curation. Xiaohe Jiang: methodology, conceptualization. Hai Qiu: formal analysis. Yu-Chia Chang: visualization, investigation. Yu-Ting Chueh: data curation. Lan Yuan: writing – review and editing, investigation. Yujun Liang: visualization, investigation. Jianguo Chang: methodology, funding acquisition. Gui Yang: supervision, resources. Sung-Fu Hung: writing – review and editing, visualization, investigation, funding acquisition. Chuang Han: writing – review and editing, supervision, resources, funding acquisition.

Conflicts of interest

There are no conflicts to declare.

Data availability

The data supporting this article have been included as part of the SI. Supplementary information: Tables S1–S7, Fig. S1–S31,

DFT computational method and further experimental details. See DOI: https://doi.org/10.1039/d6mh00152a.

Acknowledgements

The supports from the National Natural Science Foundation of China (52572329, 22302182, 22102126), the Natural Science Foundation of Hubei Province (2023AFB091), the "CUG Scholar" Scientific Research Funds at China University of Geosciences (Wuhan) (Project No. 2022187), the Key Research Project of the Anhui Provincial Key Laboratory of Green Carbon Chemistry (AHGC2025005), and the National Science and Technology Council, Taiwan (Contract No. NSTC 113-2628-M-A49-008) are gratefully acknowledged. We also thank Dr Mingxing Gong for STEM characterizations and discussions, and the support from the Yushan Young Scholar Program and the Center for Emergent Functional Matter Science, Ministry of Education, Taiwan.

References

1 J. Tian, Y. Zhang, L. Du, Y. He, X.-H. Jin, S. Pearce, J.-C. Eloi, R. L. Harniman, D. Alibhai and R. Ye, *Nat. Chem.*, 2020, **12**, 1150–1156.
2 X. Li, Y. Sun, J. Xu, Y. Shao, J. Wu, X. Xu, Y. Pan, H. Ju, J. Zhu and Y. Xie, *Nat. Energy*, 2019, **4**, 690–699.
3 H. Zhang, Y. Wang, S. Zuo, W. Zhou, J. Zhang and X. W. D. Lou, *J. Am. Chem. Soc.*, 2021, **143**, 2173–2177.
4 M. Z. Rahman, T. Edvinsson and J. Gascon, *Nat. Rev. Chem.*, 2022, **6**, 243–258.
5 S. Lin, Y. Zhang, Y. You, C. Zeng, X. Xiao, T. Ma and H. Huang, *Adv. Funct. Mater.*, 2019, **29**, 1903825.
6 W. Wang, Y. Tao, J. Fan, Z. Yan, H. Shang, D. L. Phillips, M. Chen and G. Li, *Adv. Funct. Mater.*, 2022, **32**, 2201357.
7 K. Doudrick, T. Yang, K. Hristovski and P. Westerhoff, *Appl. Catal., B*, 2013, **136**, 40–47.
8 H. Xu, X. She, T. Fei, Y. Song, D. Liu, H. Li, X. Yang, J. Yang, H. Li and L. Song, *ACS Nano*, 2019, **13**, 11294–11302.
9 K. Iwashina, A. Iwase, Y. H. Ng, R. Amal and A. Kudo, *J. Am. Chem. Soc.*, 2015, **137**, 604–607.
10 S. Wang, T. Wu, S. Wu, J. Guo, T. He, Y. Wu, W. Yuan, Z. Zhang, Y. Hua and Y. Zhao, *Angew. Chem., Int. Ed.*, 2023, **62**, e202311082.
11 J. Lin, Y. Wang, W. Tian, H. Zhang, H. Sun and S. Wang, *ACS Catal.*, 2023, **13**, 11711–11722.
12 H. Wen, L.-Y. Gan, H.-B. Dai, X.-P. Wen, L.-S. Wu, H. Wu and P. Wang, *Appl. Catal., B*, 2019, **241**, 292–298.
13 J. Carvalho Jr, C. Bressan and J. Ferreira, *Energy*, 1988, **13**, 149–152.
14 C. Feng, M. Lv, J. Shao, H. Wu, W. Zhou, S. Qi, C. Deng, X. Chai, H. Yang and Q. Hu, *Adv. Mater.*, 2023, **35**, 2305598.
15 A. U. Nwankwoala, N. O. Egiebor and K. Nyavor, *Biodegradation*, 2001, **12**, 1–10.
16 Y.-y Li, L. Lin, X. Huang and X.-y Li, *Chem. Eng. J.*, 2023, **470**, 144268.
17 J. Li, Y. Li, J. Wang, C. Zhang, H. Ma, C. Zhu, D. Fan, Z. Guo, M. Xu and Y. Wang, *Adv. Funct. Mater.*, 2022, **32**, 2109439.
18 X. Fu, D. Cheng, C. Wan, S. Kumari, H. Zhang, A. Zhang, H. Huyan, J. Zhou, H. Ren and S. Wang, *Adv. Mater.*, 2023, **35**, 2301533.
19 Y. Hu, T. Chao, Y. Li, P. Liu, T. Zhao, G. Yu, C. Chen, X. Liang, H. Jin and S. Niu, *Angew. Chem., Int. Ed.*, 2023, **135**, e202308800.
20 W. Zhu, A. G. Naidu, Q. Wu, H. Yan, M. Zhao, Z. Wang and H. Liang, *Chem. Eng. Sci.*, 2022, **258**, 117769.
21 H.-C. Eun, J.-Y. Jung, S.-Y. Park, J.-S. Park, N.-O. Chang, S.-B. Kim and B.-K. Seo, *Int. J. Environ. Res.*, 2020, **14**, 385–391.
22 J. Li, Y. Li, J. Wang, C. Zhang, H. Ma, C. Zhu, D. Fan, Z. Guo, M. Xu, Y. Wang and H. Ma, *Adv. Funct. Mater.*, 2022, **32**, 2109439.
23 Y. Liu, J. Zhang, Y. Li, Q. Qian, Z. Li, Y. Zhu and G. Zhang, *Nat. Commun.*, 2020, **11**, 1853.
24 Q. Qian, J. Zhang, J. Li, Y. Li, X. Jin, Y. Zhu, Y. Liu, Z. Li, A. El-Harairy and C. Xiao, *Angew. Chem., Int. Ed.*, 2021, **133**, 6049–6058.
25 R. Das, S. Chakraborty and S. C. Peter, *ACS Energy Lett.*, 2021, **6**, 3270–3274.
26 C. Hu, Y. Zhang, A. Hu, Y. Wang, X. Wei, K. Shen, L. Chen and Y. Li, *Adv. Mater.*, 2023, **35**, 2209298.
27 X. Guan, Q. Wu, H. Li, S. Zeng, Q. Yao, R. Li, H. Chen, Y. Zheng and K. Qu, *Appl. Catal., B*, 2023, **323**, 122145.
28 D. Liu, T. Ding, L. Wang, H. Zhang, L. Xu, B. Pang, X. Liu, H. Wang, J. Wang and K. Wu, *Nat. Commun.*, 2023, **14**, 1720.
29 X. Li, W. Bi, L. Zhang, S. Tao, W. Chu, Q. Zhang, Y. Luo, C. Wu and Y. Xie, *Adv. Mater.*, 2016, **28**, 2427–2431.
30 X. Shi, C. Dai, X. Wang, J. Hu, J. Zhang, L. Zheng, L. Mao, H. Zheng and M. Zhu, *Nat. Commun.*, 2022, **13**, 1287.
31 N. Luo, T. Montini, J. Zhang, P. Fornasiero, E. Fonda, T. Hou, W. Nie, J. Lu, J. Liu, M. Heggen, L. Lin, C. Ma, M. Wang, F. Fan, S. Jin and F. Wang, *Nat. Energy*, 2019, **4**, 575–584.
32 S. Zhang, Z. Zhang, Y. Si, B. Li, F. Deng, L. Yang, X. Liu, W. Dai and S. Luo, *ACS Nano*, 2021, **15**, 15238–15248.
33 J. Wang, C. Yang, L. Mao, X. Cai, Z. Geng, H. Zhang, J. Zhang, X. Tan, J. Ye and T. Yu, *Adv. Funct. Mater.*, 2023, **33**, 2213901.
34 Y. Cao, L. Guo, M. Dan, D. E. Doronkin, C. Han, Z. Rao, Y. Liu, J. Meng, Z. Huang and K. Zheng, *Nat. Commun.*, 2021, **12**, 1675.
35 Y. Cao, L. Guo, M. Dan, D. E. Doronkin, C. Han, Z. Rao, Y. Liu, J. Meng, Z. Huang, K. Zheng, P. Chen, F. Dong and Y. Zhou, *Nat. Commun.*, 2021, **12**, 1675.
36 S. Liu, N. Zhang, Z.-R. Tang and Y.-J. Xu, *ACS Appl. Mater. Interfaces*, 2012, **4**, 6378–6385.
37 Y. Wang, X. Liu, X. Han, R. Godin, J. Chen, W. Zhou, C. Jiang, J. F. Thompson, K. B. Mustafa and S. A. Shevlin, *Nat. Commun.*, 2020, **11**, 2531.
38 Y. Li, T. Qin, Y. Wei, J. Xiong, P. Zhang, K. Lai, H. Chi, X. Liu, L. Chen and X. Yu, *Nat. Commun.*, 2023, **14**, 7149.
39 A. Talebian-Kiakalaieh, M. Guo, E. M. Hashem, B. Xia, Y. Jiang, C. Chuah, Y. Tang, P. Kwong, J. Ran and S.-Z. Qiao, *Adv. Energy Mater.*, 2023, **13**, 2301594.
40 B. Zhu, J. Sun, Y. Zhao, L. Zhang and J. Yu, *Adv. Mater.*, 2024, **36**, 2310600.

41 W. Li, X. Zheng, B. B. Xu, Y. Yang, Y. Zhang, L. Cai, Z. J. Wang, Y. F. Yao, B. Nan and L. Li, *Angew. Chem., Int. Ed.*, 2024, e202320014.
42 H. Peng, T. Yang, H. Lin, Y. Xu, Z. Wang, Q. Zhang, S. Liu, H. Geng, L. Gu and C. Wang, *Adv. Energy Mater.*, 2022, **12**, 2201688.
43 H. M. Wasana, G. D. Perera, P. D. S. Gunawardena, P. S. Fernando and J. Bandara, *Sci. Rep.*, 2017, **7**, 42516.
44 Y. Wang, Y. Wang and R. Xu, *J. Phys. Chem. C*, 2013, **117**, 783–790.
45 P. Wang, J. Zheng, X. Xu, Y. Q. Zhang, Q. F. Shi, Y. Wan, S. Ramakrishna, J. Zhang, L. Zhu and T. Yokoshima, *Adv. Mater.*, 2024, **36**, 2404806.
46 J. Jia, D. Li, X. Cheng, J. Wan and X. Yu, *Appl. Catal., A*, 2016, **525**, 128–136.
47 S. Zhan, F. Zhou, N. Huang, Y. Liu, Q. He, Y. Tian, Y. Yang and F. Ye, *Appl. Surf. Sci.*, 2017, **391**, 609–616.
48 H.-W. Tseng, M. B. Wilker, N. H. Damrauer and G. Dukovic, *J. Am. Chem. Soc.*, 2013, **135**, 3383–3386.
49 J. Guan, K. Koizumi, N. Fukui, H. Suzuki, K. Murayama, R. Toyoda, H. Maeda, K. Kamiya, K. Ohashi and S. Takaishi, *ACS Catal.*, 2024, **14**, 1146–1156.
50 R. Yin, Z. Wang, J. Zhang, W. Liu, J. He, G. Hu and X. Liu, *Small Methods*, 2025, **9**, 2401976.
51 B. Yan, D. Liu, X. Feng, M. Shao and Y. Zhang, *Adv. Funct. Mater.*, 2020, **30**, 2003007.
52 Y. Zhu, Y. Chen, Y. Feng, X. Meng, J. Xia and G. Zhang, *Adv. Mater.*, 2024, **36**, 2401694.
53 A. Mukherji, R. Marschall, A. Tanksale, C. Sun, S. C. Smith, G. Q. Lu and L. Wang, *Adv. Funct. Mater.*, 2011, **21**, 126–132.
54 A. Talebian-Kiakalaieh, M. Guo, E. M. Hashem, B. Xia, Y. Jiang, C. Chuah, Y. Tang, P. Kwong, J. Ran and S. Z. Qiao, *Adv. Energy Mater.*, 2023, **13**, 2301594.
55 Y. Hu, T. Chao, Y. Dou, Y. Xiong, X. Liu and D. Wang, *Adv. Mater.*, 2025, 2418504.
56 Q. Kang, T. Wang, P. Li, L. Liu, K. Chang, M. Li and J. Ye, *Angew. Chem., Int. Ed.*, 2015, **54**, 841–845.
57 J. Wang, X. Guan, H. Li, S. Zeng, R. Li, Q. Yao, H. Chen, Y. Zheng and K. Qu, *Nano Energy*, 2022, **100**, 107467.
58 C. Wang, J. Li, Y. Yuan, B. Ouyang, Z. Guo, C. Lin, X. Yang, B. Kang, C. Li, Y. Sun and K. Xu, *Angew. Chem., Int. Ed.*, 2025, **64**, e202505616.
59 H. Yu, Y. Xuan, Q. Zhu and S. Chang, *Green Chem.*, 2023, **25**, 596–605.
60 J. Li, W. Pan, Q. Liu, Z. Chen, Z. Chen, X. Feng and H. Chen, *J. Am. Chem. Soc.*, 2021, **143**, 6551–6559.
61 X. Li, L. Li, G. Chen, X. Chu, X. Liu, C. Naisa, D. Pohl, M. Löffler and X. Feng, *Nat. Commun.*, 2023, **14**, 4034.